RSC Advances

PAPER

View Article Online
View Journal | View Issue

Cite this: *RSC Adv.*, 2018, **8**, 5749

Surfactant-assisted hydrothermal synthesis of rGO/$SnIn_4S_8$ nanosheets and their application in complete removal of Cr(VI)†

Pingfan Xu,[a] Siyi Huang,[b] Yuancai Lv,[b] Yi Chen,[ac] Minghua Liu *[b] and Haojun Fan *[ac]

To solve the problem of contamination of hexavalent chromium (Cr(VI)), visible-light-driven graphene-based ternary metal chalcogenide nanosheets (rGO/$SnIn_4S_8$) were synthesized *via* a one-pot surfactant-assisted hydrothermal method for the photoreduction of Cr(VI). Characterizations demonstrated that $SnIn_4S_8$ nanosheets were uniformly distributed on the surface of rGO and the as-synthesized nanosheets exhibited excellent photocatalytic activity under visible light. In addition, the effects of pH, concentration of critic acid, holes and electron scavengers on the reduction of Cr(VI) were systematically investigated. It was found that 50 mg L^{-1} of Cr(VI) could be completely removed within 30 min at pH 2 when citric acid served as a hole scavenger. Kinetic studies showed that the photocatalytic reduction of Cr(VI) processes obeyed the pseudo first order model. Further study indicated that the Cr(III) species was immediately adsorbed onto the surface of the rGO/$SnIn_4S_8$ nanosheets after photocatalytic reduction of Cr(VI). Additionally, recycling results suggested that rGO/$SnIn_4S_8$ nanosheets possessed high recycle ability and stability after repeated use (5 times). This effective and promising work might provide a new strategy for the photoreduction of Cr(VI) and complete removal of chromium from effluent through the novel photocatalyst rGO/$SnIn_4S_8$.

Received 29th November 2017
Accepted 22nd January 2018

DOI: 10.1039/c7ra12863k

rsc.li/rsc-advances

1 Introduction

Chromium is a common chemical element in the earth's crust which has been widely used in various industries, *e.g.* leather tanning, electroplating, textile dye manufacturing and wood preservation.[1–3] Over the past decades, considerable quantities of effluent containing chromium have been discharged into the aqueous environment, which caused serious environmental problems and harmful effects to human beings. Hence, concern over chromium contamination of the environment and the requirement for the safe disposal of chromium waste is a hot topic of current interest.[4]

Chromium exists in several forms but predominantly is present as two stable oxidation states in water: trivalent chromium (Cr(III)), which is an essential nutrient for glucose and protein metabolism, and hexavalent chromium (Cr(VI)), which is artificially produced for use in industrial processes and rarely found in nature.[5] Cr(III) forms yield relative insolubility at pH ≥ 4 with no-toxicity and won't cross the cell membranes. On the contrary, Cr(VI) shows high water-solubility and environmental mobility, thus it has high permeability in cell membranes and presents acute toxicity, teratogenicity and carcinogenicity.[6,7] Therefore, the reduction of Cr(VI) originated from effluent into Cr(III) is extremely necessary for natural environment.

The most widely used treatment process for the removal of Cr(VI) is the chemical reduction followed by precipitation, whereas this process consumes large amounts of reducing agent and generates large quantities of chromium containing sludge, which has been listed as hazardous wastes.[8] Recent developed technologies for the remediation of Cr(VI) including microbial degradation, membrane process, ion exchange, absorptive method and electrochemical precipitation,[9–13] nevertheless, those strategies either require huge investment, or consume large amounts of energy and chemical agent. Hence, it is urgent to seek out an effective and low-cost strategy for removing Cr(VI) without secondary pollution. Heterogeneous photocatalysis has been recognized as a promising for chromium removal due to its high efficiency, low energy consumption and mild reaction condition. However, the traditional photocatalyst such as TiO_2, ZnO and SnO_2, usually have wide band gap energy and fail to be irradiated under visible light.[14,15] Moreover, those power photocatalysts usually have a limitation of surface area which results in a low adsorption of metal ion on the surface of photocatalysts.[16] Therefore, it is essential to develop a high specific surface area, visible-light responsive photocatalyst for removal of chromium.

[a]*National Engineering Laboratory for Clean Technology of Leather Manufacture, Sichuan University, Chengdu 610065, China. E-mail: fanhaojun@scu.edu.cn*

[b]*College of Environment & Resource, Fuzhou University, Fuzhou 350116, P. R. China. E-mail: mhliu2000@fzu.edu.cn*

[c]*Light Industry, Textile and Food Institution, Sichuan University, Chengdu 610065, China*

† Electronic supplementary information (ESI) available. See DOI: 10.1039/c7ra12863k

Metal chalcogenides (MC), which possess narrow band gap and visible-light absorption, has received recent attention as a new two-dimensional (2D) layered nanomaterials.[17] In the past few years, significant efforts have been devoted to binary metal chalcogenides, such as MoS_2, CdS, SnS_2 and WS_2.[18] In this family, most binary compounds have unfavorable band gap or band position, however, ternary metal chalcogenides show a high flexibility for tuning the band gap and energy levels.[19] For instance, tin indium sulfide ($SnIn_4S_8$) as a novel ternary chalcogenide semiconductor has exhibited potential application in photocatalytic reduction of heavy metal ion. But single $SnIn_4S_8$ semiconductor owns a small specific surface area and fast electron–hole recombination,[20] which result in the decrease of photocatalytic activity. Graphene with one-atom-thick layer and two-dimensional nano scale of sp^2-bonded carbon structure, taking advantage of higher surface activity and specific surface area per unit volume, has been applied to combine with semiconductor photocatalysts such as TiO_2, Fe_3O_4, $Gd(OH)_3$, CdS and $CuInS_2$.[21–23] In those hybrid systems, the graphene serves as both the supported carrier of photocatalyst and the adsorption active site, which extremely promotes the photocatalytic activity of the graphene–semiconduct hybrid. Among the graphene analogues, rGO has been widely utilized due to its facile synthesis and easy modification.[24] Despite being chemically or hydrothermally reduced, the rGO sheets still have some oxygen functional groups such as hydroxyl and carboxyl groups, which could capture the heavy metal ion.[25,26] Thus, it provides a new strategy for simultaneous photocatalysis of Cr(VI) and adsorption of Cr(III). Previous studies have demonstrated that graphene-based material could greatly improve photocatalytic efficiency of Cr(VI) to Cr(III) because of the synergy of graphene with semiconduct hybrid.[27,28] In this regard, a few reports on the photocatalytic reduction of Cr(VI) over graphene-based material such as α-FeOOH nanorod/RGO, α-MnO_2@RGO, SnS_2/RGO have already been reported.[29–31] To the best of our knowledge, few groups have reported the concurrence of photocatalysis of Cr(VI) and adsorption of Cr(III) by the graphene-based material.

Following this idea, herein, an attempt was carried out to construct the layer ternary metal chalcogenide coupling with reduced graphene oxide (rGO) using a facile surfactant-hydrothermal synthesis (see Scheme 1) to further enhance the photocatalytic activity of metal chalcogenides photocatalyst. In this case, rGO could act as both the enhancement of adsorption capacity and the photocatalysis activity, while MC in the hybrids could serve as active sites for photocatalytic reaction, as a result, the as-fabricated rGO/$SnIn_4S_8$ nanosheets exhibited significant improvement on the photocatalytic activity for the reduction of Cr(VI) to Cr(III) under visible light irradiation. Simultaneously, a more profound study was provided to explain the promoted and inhibited reduction mechanism for photocatalysis of Cr(VI) based on the complexity of wastewater. Several influence factors, such as pH, concentration of citric acid, the species of hole scavenger and electron scavenger, were investigated to reveal the mechanism and optimize condition for photocatalytic reduction of Cr(VI). In addition, the simultaneous adsorption of Cr(III) on the surface of rGO/$SnIn_4S_8$ was confirmed to interpret the synergetic mechanism of photocatalysis and adsorption of rGO/$SnIn_4S_8$. Finally, the stability and reusability of photocatalyst of the as-fabricated nanosheets were investigated.

2 Experimental

2.1 Materials

Tin(IV) chloride pentahydrate ($SnCl_4 \cdot 5H_2O$), indium(III) chloride tetrahydrate ($InCl_3 \cdot 4H_2O$) and thioacetamide (TAA) were obtained from Aladdin Ltd, China. Natural graphite flakes with an average particle size of 100 meshes, potassium dichromate, phosphorus pentoxide and sodium dodecylbenzene sulfonate (SDBS) were purchased from Sinopharm Chemical Reagent co. Ltd, China. All the reagents were of analytical grade and used as received without further purification.

2.2 Preparation of graphene oxide

Graphene oxide (GO) was synthesized by the modified Hummers' method.[32] Briefly, natural graphite flakes (10.0 g) was preoxidized in a mixture of concentrated H_2SO_4 (50 ml), $K_2S_2O_8$ (10.0 g) and P_2O_5 (10.0 g) stirring at 80 °C for 4.5 h in a water bath. The pre-oxidized graphite was washed with excess deionized water *via* repeated filtration until the filtrate water become neutral, and then dried in a vacuum oven. The pre-oxidized graphite (2.0 g) was dispersed in concentrated H_2SO_4 (92 ml) in an ice bath, then $KMnO_4$ (12.0 g) was gradually added to keep the bath temperature below 10 °C. The mixture was transferred to 35 °C bath for 2 h and was cooled down in ice bath, then 184 ml deionized water was added dropwisely to prevent the temperature rising sharply. Subsequently, the

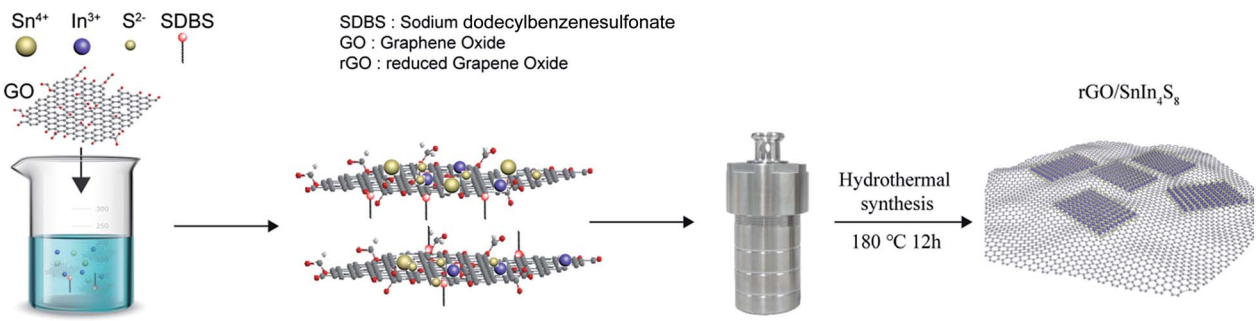

Scheme 1 Schematic illustration of the synthetic procedure of rGO/$SnIn_4S_8$ nanosheets.

reaction was heated at 75 °C for 4 h, then the black product was reacted with H_2O_2 until the suspension turn bright yellow. Finally, the product was washed with 5% HCl and deionized water, then freeze-dried for further used.

2.3 Synthesis of rGO/$SnIn_4S_8$

rGO/$SnIn_4S_8$ was synthesized using a one-pot surfactant-assisted hydrothermal method. In a typical synthesis procedure, 10 mg GO, 0.6 mmol $SnCl_4 \cdot 5H_2O$ (dissolved in 2 ml acetic acid), 2.4 mmol $InCl_3 \cdot 4H_2O$ and 0.021 mmol SDBS were dissolved in 70 ml deionized water and the mixture was sonicated at room temperature for 10 min, and then vigorously stirred for 30 min to ensure homogeneous dispersion. Finally, 4.8 mmol TAA was added to the reaction system and kept stirring for 10 min. The solution was introduced into a 100 ml Teflon-lined stainless steel autoclave and maintained at 180 °C for 12 h. After cooling down to room temperature, the product was collected by filtration, and washed repeatedly by deionized water and anhydrous ethanol, finally freeze-dried to obtain the rGO/$SnIn_4S_8$ nanosheets. Pure rGO and $SnIn_4S_8$ were also prepared under the same experimental condition.

2.4 Characterization

The morphology of the samples were visualized using a field emission scanning electron microscopy (FESEM, Nova Nano SEM450, FEI, America, operated at 20 kV) and a high resolution transmission electronic micrograph (HRTEM, Tecnai G220, FEI, America, operated at 200 kV). The crystalline phase of the samples were analyzed by a powder X-ray diffractometer (XRD) (Miniflex600, Rigaku, Japan) at 40 kV and 15 mA with Ni-filtered Cu Kα irradiation ($\lambda = 1.5406$ Å). The surface composition and chemical state of the photocatalyst were measured by X-ray photoelectron spectroscopy (XPS, ESCA Lab250, Thermo Scientific Ltd, America) with Al Kα radiation in twin anode, where the binding energies were calibrated by referencing C 1s (284.6 eV) peak. The UV-Vis diffuse reflectance spectra (DRS) were recorded on a UV-Vis spectrophotometer (UV-2450, Shimadzu, Japan) using $BaSO_4$ as reference. Brunauer–Emmett–Teller (BET) specific surface area was investigated by ultrapure nitrogen adsorption/desorption experiments at the boiling temperature of liquid nitrogen (77 K) on an ASAP 2020 Accelerated Specific Surface Area and Porosimetry Analyzer. Prior to BET measure, the sample was degassed under vacuum condition at 120 °C for 8 h. Cr(VI) was determined using the diphenylcarbazide (DPZ) method at 540 nm on a continuous flow analyzer (SEAL Analytical, Germany). Total chromium was measured using an inductively coupled plasma optical emission spectrometer (ICP-OES, Optima 8000, PerkinElmer, America). Fourier-transform infrared spectra (FT-IR) were recorded with a Thermo Scientific Nicolet iS10 using KBr pellets technique over the wavenumber ranging from 4000 to 400 cm^{-1}.

2.5 Photocatalysis and adsorption experiment

All photocatalytic runs were carried out in a double-walled quartz jacket filled with cool water under visible light irradiation. A 300 W xenon lamp (Beijing Aulight Ltd, China) coupled with a cutoff filter ($\lambda > 420$ nm) was used as the irradiation source. Photocatalytic activity of the sample was evaluated through the experiment of photocatalytic reduction of Cr(VI) under visible light irradiation. In a typical procedure, 10 mg of catalyst was dispersed in 50 ml of Cr(VI) solution, the initial concentration (C_0) of which was 50 mg L^{-1}. Subsequently, the suspension was magnetically stirred in the dark for 30 min to ensure the adsorption–desorption equilibrium between reactants and photocatalysts. Then, the above suspension was irradiated by Xe lamp (10 cm away from the photocatalytic reactor), during this period, 3 ml of suspension was sampled at a specific time intervals and then centrifuged to remove the catalysts. The concentration of Cr(VI) was determined on a continuous flow analyzer. Consequently, the photocatalytic efficiency of Cr(VI) can be calculated according to C/C_0, where C_0 is the concentration of after adsorption equilibrium and C is the concentration of Cr(VI) after reaction.

The synergy of photocatalysis and adsorption experiment was divided into two parts. Firstly, the photocatalytic reduction was performed as mentioned above. Secondly, the system was transferred to a thermostatic reciprocating shaker at 200 rpm in 30 °C. The residual total concentrations of chromium and Cr(VI) was measured by ICP-OES and continuous flow analyzer. Then Cr(III) concentration in the liquid could be calculated from the concentration difference between total chromium and Cr(VI). The adsorption capacity (q_t, mg g^{-1}) could be calculated from the following equation:

$$q_t = \frac{C_0 - C_t}{m} \times V \quad (1)$$

where C_0 and C_t are the initial and concentrations of Cr(VI) and total chromium (mg L^{-1}), respectively, while V is the volume of solution (ml), and m is the mass of rGO/$SnIn_4S_8$ (g).

2.6 Recycling experiment

To evaluate the stability of the photocatalyst, the used photocatalyst was regenerated by filtration after the photocatalytic reaction and washed with deionized water and diluted HCl (10%, v/v) for 3–4 times until complete removal of chromium from photocatalyst, and then the photocatalyst was dried at 80 °C for the next run of photoreaction under the same conditions.

3 Results and discussion

3.1 Crystal and morphological characterization

XRD analysis was carried out to investigate the purity and crystallinity of the $SnIn_4S_8$ sample. As shown in Fig. 1a, the diffraction pattern of rGO/$SnIn_4S_8$ exhibited 13 peaks at 14.3°, 23.4°, 27.5°, 28.8°, 33.3°, 41.1°, 43.7°, 47.8°, 50.2°, 56.0°, 59.5°, 66.8° and 69.9°, corresponding to (111), (220), (311), (222), (400), (422), (333), (440), (531), (533), (444), (553) and (880) of crystal plane of pristine $SnIn_4S_8$, respectively. In addition, a small peak in rGO/$SnIn_4S_8$ appeared at 26°, which belonged to the (100) plane diffraction peak of rGO. All the reflections in the diffraction patterns of as-synthesized rGO/$SnIn_4S_8$ were well indexed with pure cubic phase of $SnIn_4S_8$ (JCPDS card #42-1305,

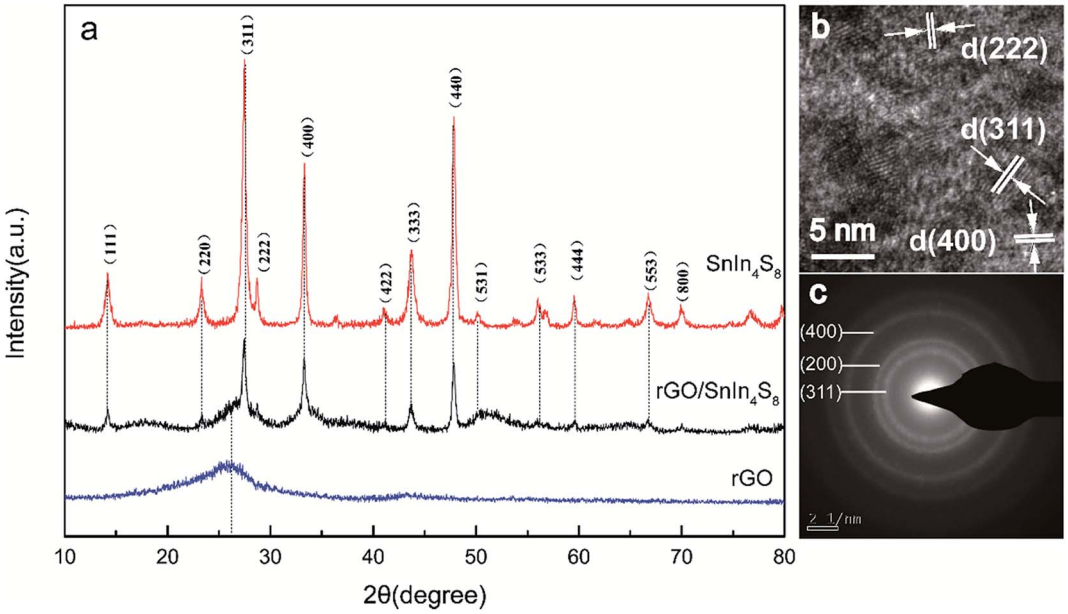

Fig. 1 (a) XRD pattern of pure $SnIn_4S_8$, rGO and rGO/$SnIn_4S_8$; (b) high resolution TEM images of the lattice fringer and (c) electron diffraction pattern of rGO/$SnIn_4S_8$.

$a = b = c = 10.751$ Å). The TEM image of rGO/$SnIn_4S_8$ in Fig. 1b and c clearly showed that $SnIn_4S_8$ aggregated on the surface of rGO sheet and the spacing distance of lattice fringe was well-matched the crystal plane of (222), (311), (400) of pristine $SnIn_4S_8$. The high diffraction intensity and clear lattice fringer of rGO/$SnIn_4S_8$ indicated that the $SnIn_4S_8$ was well crystallized on the rGO surface *via* the surfactant-assisted hydrothermal synthesis.

The morphology of rGO, pure $SnIn_4S_8$ and rGO/$SnIn_4S_8$ were illustrated in Fig. 2. Obviously, SEM image of rGO sheets exhibited a wrinkle ultrathin nanosheet structure with a relative smooth surface. On the contrary, pure $SnIn_4S_8$ nanosheet displayed a rough surface, aggregating disorderly to form a formicary-like superstructure. In the case of rGO/$SnIn_4S_8$, $SnIn_4S_8$ nanosheets were uniformly distributed on the surface of rGO to form a wrinkled-like nanosheet.

A typical transmission electron microscopy (TEM) and high resolution TEM (HRTEM) images of the as-synthesized rGO/$SnIn_4S_8$ were characterized to further reveal the morphology and crystal structure. As shown in Fig. 2d and f, $SnIn_4S_8$ nanosheets were paved on the surface of rGO. Further crystallographic orientations of $SnIn_4S_8$ were confirmed from HRTEM analysis by studying the lattice plane stacked on the surface of rGO. Distinctive sets of lattice fringes were lying on flat on the surface of rGO which corresponded to the lattice planes of (222), (311), (400) and (111) of the $SnIn_4S_8$, respectively. TEM and HRTEM images further demonstrated that the as-prepared $SnIn_4S_8$ with well crystallinity was stacked on the surface of rGO to form a nanocomposite heterojunction.

Herein, rGO provided both the supported carrier of $SnIn_4S_8$ and promoted the separation of photogenerated electron–holes pair in heterojunction.[33,34] Moreover, rGO played a role in the aggregation of crystallites because the surface functional group could serve as a matrix or ligand for various anion.[35] In this case, it is evidenced that the $SnIn_4S_8$ particle is apt to nucleate on the surface of rGO and aggregated in crystalline along rGO sheets.

3.2 XPS surface element analysis

The chemical states of C, S, In and Sn element were characterized by X-ray photoelectron spectroscopy (XPS). As expected, the characteristic peak of C 1s, S 2p, In 3d and Sn 3d were confirmed according the XPS survey scan. As shown in Fig. 3b, the C 1s core-level spectrum of rGO/$SnIn_4S_8$ nanosheets was fitted into three main characteristic peaks with binding energies at 284.8, 286.0 and 289.4 eV corresponding to the sp^2 C–C bonds, sp^3 C–O bonds and sp^2 C=O bonds, respectively. Fig. 3d displayed the S 2p core-level spectrum with two peaks, which were respectively assigned to In–S and Sn–S bond. The In 3d spectrum exhibited two intense peaks at 445.2 and 452.8 eV corresponding respectively to $3d_{5/2}$ and $3d_{3/2}$, resulting from the spin–orbit splitting. The peak area ratio and the spin orbital splitting of In $3d_{5/2}$ and In $3d_{3/2}$ were 1.47 and 7.6 eV, which confirmed the In^{3+} oxidation state of the In element in the sample. At the same time, the peak area ratios and the spin orbital splitting of Sn $3d_{5/2}$ and Sn $3d_{3/2}$ were 1.47 and 8.4 eV, which was the characteristic peak of Sn^{4+}.

3.3 Surface area of photocatalyst

Generally, photocatalytic activity of photocatalyst is strongly dependent on the surface area. Large surface area is likely to exhibit excellent photocatalytic activity, because a large surface area provides more active sites for adsorbing pollutant.[36] The Brunauer–Emmett–Teller (BET) analysis was carried out to determine the surface area of rGO, $SnIn_4S_8$ and rGO/$SnIn_4S_8$. As shown in the ESI (Fig. S1, ESI†), special surface areas followed

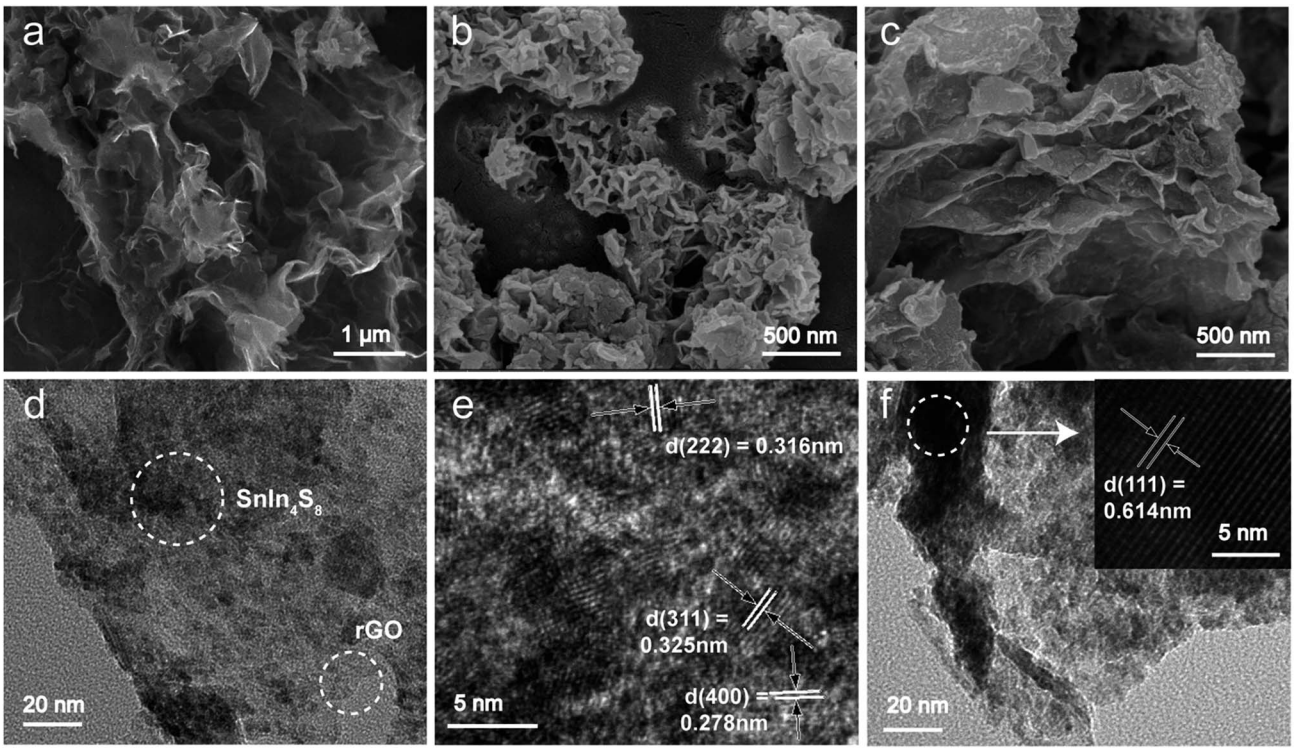

Fig. 2 SEM image of (a) rGO, (b) $SnIn_4S_8$ and (c) rGO/$SnIn_4S_8$; (d) TEM image of rGO/$SnIn_4S_8$; (e and f) HRTEM image of the lattice fringes of $SnIn_4S_8$ on the surface of rGO.

an order of rGO (212.8 $m^2 g^{-1}$) > rGO/$SnIn_4S_8$ (109.0 $m^2 g^{-1}$) > $SnIn_4S_8$ (64.8 $m^2 g^{-1}$), which revealed that the special surface areas of $SnIn_4S_8$ increased after supported by rGO. According to IUPAC classification of 1985, the physisorption isotherms of rGO/$SnIn_4S_8$ is assigned to the reversible type IV isotherms with a H3 hysteresis loops, which clearly evidenced the nanosheets

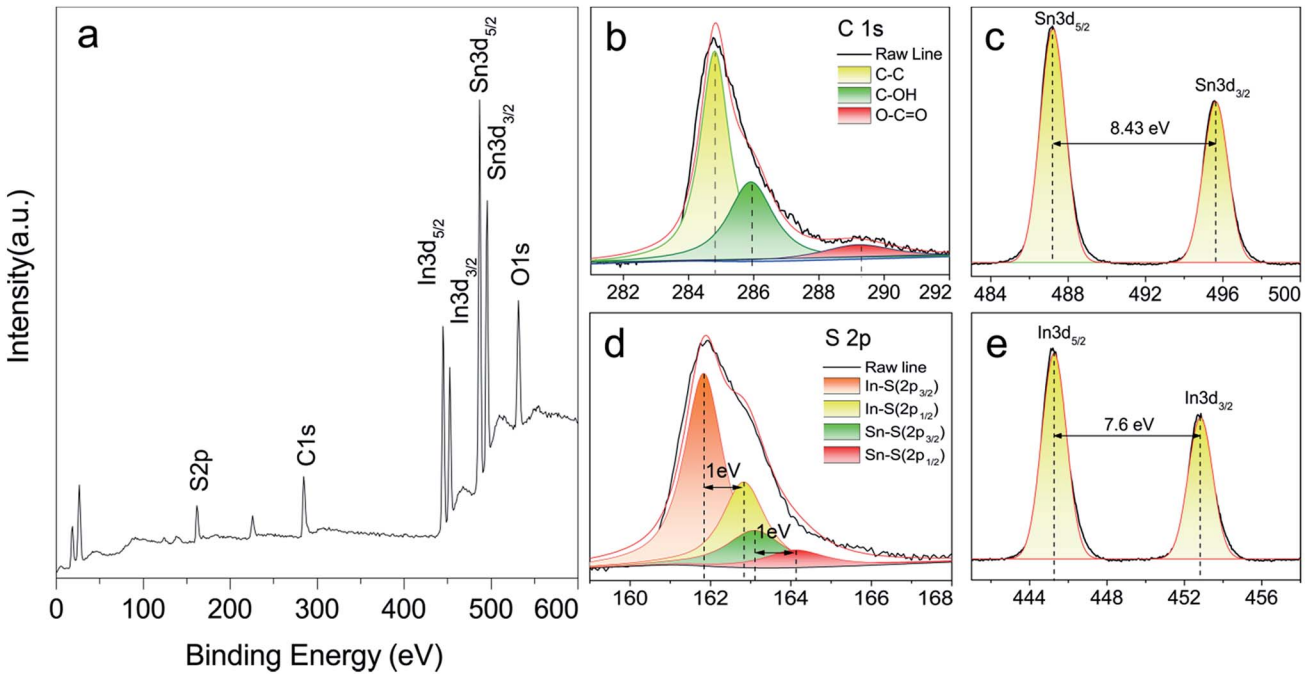

Fig. 3 XPS spectra of rGO/$SnIn_4S_8$. (a) Survey scan of rGO/$SnIn_4S_8$; (b) C 1s core-level spectrum; (c) S 2p core-level spectrum; (d) In 3d core-level spectrum; (e) Sn 3d core-level spectrum.

consisted of non-rigid aggregates of plate-like particles and the pore network was not completely filled with pore condensate.[37]

3.4 Optical properties and photocatalytic processes

The optical properties of rGO/$SnIn_4S_8$ and $SnIn_4S_8$ were characterized by UV-Vis diffuse reflectance spectra and flat-band potential. A classical Tauc approach was employed to estimate the optical band gap energy (E_g) of the rGO/$SnIn_4S_8$ and $SnIn_4S_8$ according to the following empirical equation:[38]

$$(\alpha h\nu)^n \propto (h\nu - E_g) \quad (2)$$

where α, $h\nu$ and E_g are the absorption coefficient, photon energy and bang gap, respectively. n is related to the characteristics of the transition of a semiconductor (indirect transition: $n = 1/2$; direct transition: $n = 2$). In the case of rGO/$SnIn_4S_8$, the value of n is 2 as it is a type of direct transition semiconductor.[39] Plot of $(\alpha h\nu)^2$ against $h\nu$ based on the direct transition is shown in Fig. 4b. It was found that the energy gap of rGO/$SnIn_4S_8$ and $SnIn_4S_8$ were approximately 1.85 eV and 1.98 eV, respectively. Compared with the pure $SnIn_4S_8$, a red shift of the band gap was observed for the rGO/$SnIn_4S_8$ nanosheets, which led to the shift of the fundamental absorption edge to longer wavelength, thus affecting the rate constant of photocatalytic reaction.[40] Additionally, the sample of rGO/$SnIn_4S_8$ and $SnIn_4S_8$ could absorb light over the entire UV and wide-range visible-light regions, which indicated that both them could act as a promising visible-light responsive photocatalyst.

To further investigate the conduction band edges of rGO/$SnIn_4S_8$, the flat-band potential was measured using the electrochemical method and depicted by Mott–Schottky plot. The data of $C_{SC} - V$ were used for evaluating the flat band potential by Mott–Schottky equation:

$$\frac{1}{C_{SC}} = \frac{2}{\varepsilon\varepsilon_0\ e\ N_D A^2}\left(V - V_{fb} - \frac{k_B T}{e}\right) \quad (3)$$

where C_{SC} is the space charge capacitance, ε is the dielectric constant of semiconductor, ε_0 is the vacuum permittivity, N_d denotes the donor density, T is the absolute temperature, k_B is Boltzmann's constant, V is the applied voltage. Plot of $1/C_{SC}$ against V should yield a straight line from which V_{fb} can be determined by the intercept on the V axis. As shown in Fig. 4c, the flat band potential obtained from the v-axis intercepts of the linear was −0.7 eV (*vs.* SCE), and the slopes of Mott–Schottky plots was positive, which demonstrated rGO/$SnIn_4S_8$ was n-type semiconductors.[41] Therefore, it can be deduced that rGO/$SnIn_4S_8$ composites could facilitate the efficient reduction of Cr(VI) due to its higher electron density.

Based on the measured values of flat band potential and band gap, the conduction and valence band edges of rGO/$SnIn_4S_8$ were calculated to be −0.459 eV and 1.391 eV (*vs.* SHE), respectively, which revealed that Cr(VI) can be photocatalytic

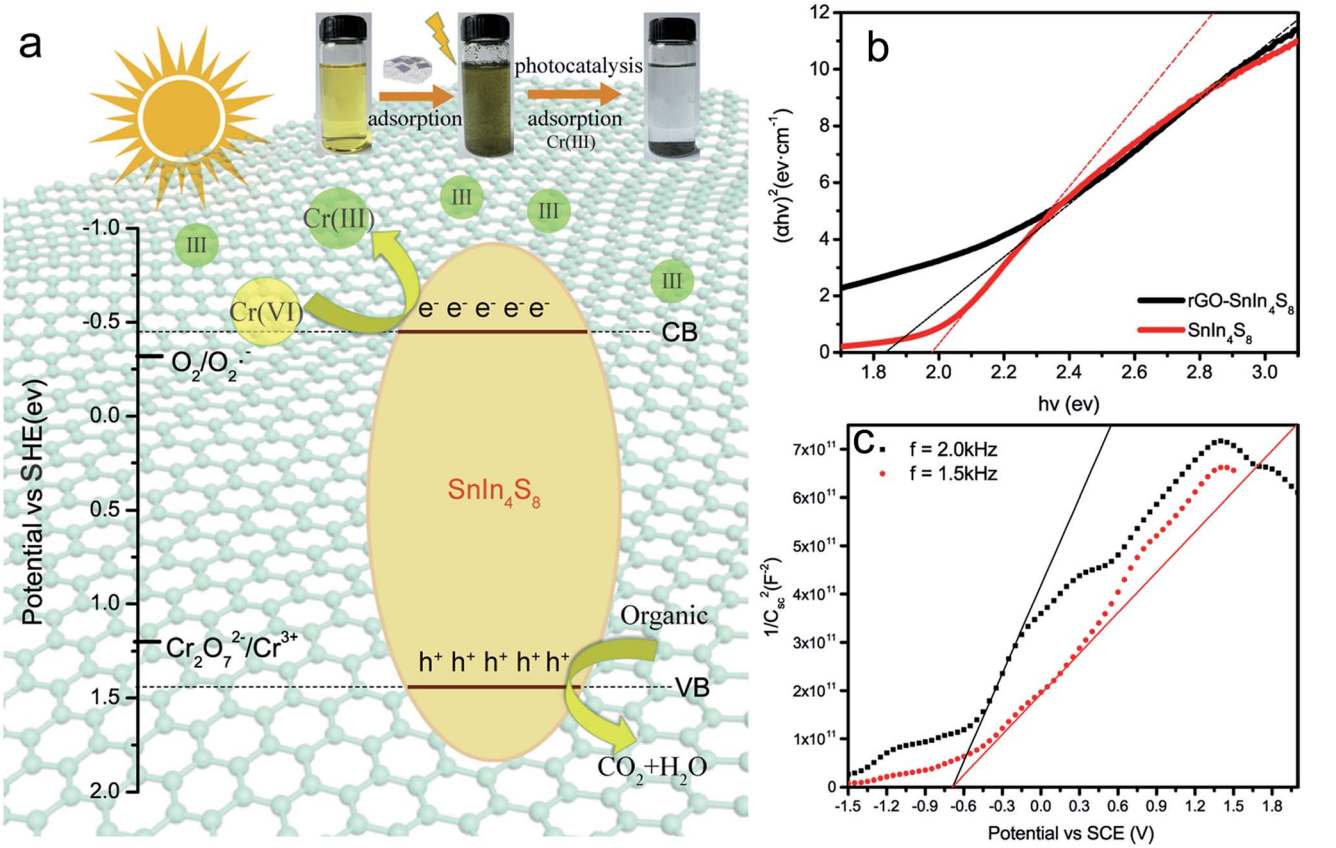

Fig. 4 (a) The photocatalytic mechanism of rGO/$SnIn_4S_8$ nanosheet and its optical structure. (b) UV-Vis diffuse reflectance spectra of pure $SnIn_4S_8$ and rGO/$SnIn_4S_8$; (c) the Mott–Schottky plots of rGO/$SnIn_4S_8$ measured at 1500 and 2000 Hz.

reduced under visible light. As shown in Fig. 4a, the electrons excited from the valence band (VB) of $SnIn_4S_8$ to the respective conduction band (CB), remaining the hole in the VB. Meanwhile, the electrons can move along the rGO surface without quenching because rGO can promote the separation of the photogenerated electron–holes pair through interfacial charge transfer.

The photocatalytic reduction of Cr(VI) can be described *via* a photocatalytic process with a simplified mechanism as follows.

$$SnIn_4S_8 + h\nu \rightarrow h^+ + e^- \quad (4)$$

$$Cr_2O_7^{2-} + 14H^+ + 6e^- \rightarrow 2Cr^{3+} + 7H_2O \quad (5)$$

$$O_2 + e^- \rightarrow {}^{\bullet}O_2^- \quad (6)$$

$${}^{\bullet}O_2^- + \text{organic} \rightarrow \cdots \rightarrow CO_2 + H_2O \quad (7)$$

$$h^+ + \text{organic} \rightarrow \cdots \rightarrow CO_2 + H_2O \quad (8)$$

3.5 Effect factors on the photocatalytic reduction of Cr(VI)

3.5.1 Effect of pH value on the photocatalytic reduction of Cr(VI). The solution acidity is one of the most important factors in the photocatalysis system. It influences not only the surface charge properties of the photocatalyst, but also metal ion adsorption on the surface of photocatalyst.[42,43] In this study, a series of experiments were conducted with a pH value ranging from 2 to 10 and adding a concentration of 20 mg L^{-1} Cr(VI) and 0.1 mM citric acid. As shown in Fig. 5a, it could be observed that the photocatalytic reduction rate of Cr(VI) depended strongly on pH. The reduction efficiency of Cr(VI) decreased gradually with the increase of pH value. At pH 2, the maximum reduction rate was achieved and 93.8% of Cr(VI) was removed within 15 min. Moreover, the kinetic studies showed that the Cr(VI) photoreduction kinetic were well fitted by the pseudo first order kinetic model and the rate constants were 0.153 min^{-1}, 0.032 min^{-1}, 0.018 min^{-1} and 0.019 min^{-1} corresponding to the pH value of 2, 4, 7 and 10, respectively. The rate constants decreased dramatically with the increase of pH value. The reason was that the dominant form of Cr(VI) were $HCr_2O_7^-$ and $Cr_2O_7^{2-}$ at acid medium, while the photocatalyst surface carried positive charge due to the adsorption of H^+ ions on the surface, the species of Cr(VI) could adsorb effectively on the surface of photocatalyst owing to the electrostatic interaction. The higher adsorption capacity results in the higher photocatalytic activity. On the contrary, the photocatalyst surface absorb plenty of OH^- at high pH, which resulted in the mutual repulsion between photocatalyst and anionic Cr(VI), thus causing a decrease of photocatalytic activity.[44,45] Further, the superior performance of the rGO/$SnIn_4S_8$ nanosheets toward photoreduction of Cr(VI) has been compared to other graphene-based whose results are listed in photocatalysts (Table S1, ESI†). The present work was able to reduced 99% of Cr(VI) (50 mg L^{-1}) within 30 min, which was outperforming the previous reported graphene-based materials.

3.5.2 Effect of concentration of citric acid on the photocatalytic reduction rate. The presence of holes scavenger such as many organic substances can lessen recombination of photogenerated electron–holes, which improves the quantum efficiency for photocatalytic reduction. Citric acid usually served as a holes scavenger to deplete the photogenerated holes from the photocatalyst.[46] In this study, citric acid was selected as a hole scavenger to evaluate the effect of different concentrations of citric acid on the photocatalytic reduction rate of Cr(VI). As shown in Fig. 5b, the photocatalytic reduction rate of Cr(VI) increased with citric acid concentration. Inspiringly, the removal efficiency of Cr(VI) could reach up to 99.8% in presence of 2 mM citric acid within 30 min, whereas the reduction rate of Cr(VI) was only 41.3% in absence of citric acid. The high correlation coefficient under different citric acid concentrations demonstrated that the Cr(VI) reduction process obeyed the pseudo-first-order model. The maximum reduction rate constant k (0.126 min^{-1}) appeared at the concentration of 2 mM citric acid, which was 8 times higher than the rate constant without citric acid.

The explanation for promoting the reduction of Cr(VI) in presence of citric acid can be ascribed to two aspects: (a) the separation of photogenerated electron–holes pair on the surface of photocatalyst;[47] (b) preventing the chromium species from oxidating by holes or hydroxyl radicals.[42] In presence of citric acid, the photogenerated electron–holes pair are spatially in isolated state, and the citric acid on one hand, can capture the photogenerated holes, on the other hand, can combine with Cr(V) to form a stable complex, all contributing to the higher Cr(VI) reduction rate. The recycle reaction can be expressed simply as follows:

$$Cr(VI) + e^- \rightarrow Cr(V) + e^- \rightarrow Cr(IV) + e^- \rightarrow Cr(III) \quad (9)$$

$$H_2O + h^+ \rightarrow {}^{\bullet}OH + H^+ \quad (10)$$

$$Cr(V)/Cr(IV)/Cr(III) + h^+({}^{\bullet}OH) \rightarrow Cr(VI)/Cr(V)/Cr(IV) + HO^- \quad (11)$$

The reaction in presence of citric acid is described as follows:

$$Cit + h^+ \rightarrow Cit^{\bullet+} \quad (12)$$

$$Cr(V) + Cit \rightarrow Cr(V) - Cit \quad (13)$$

3.5.3 Effect of hole scavenger on photocatalytic reduction rate. Sufficient evidence for trapping of photogenerated holes may be come true by the addition of hole scavenger. In the actual effluent, there are various organic compound which can act as a hole scavenger. In order to further elucidate different hole scavenger in enhancing photocatalytic reduction rate of Cr(VI), several kinds of common organic additives were added into the reaction system to elaborate their effect on Cr(VI) reduction rate, such as methanol (MeOH), ethanol (EtOH), formic acid (FA), acetic acid (HAC) and isopropanol (IPA). It can be seen in Fig. 5c that after 120 min of irradiation, the maximum removal efficiency of Cr(VI) was achieved in presence of FA. The photocatalytic reduction rate of Cr(VI) showed an

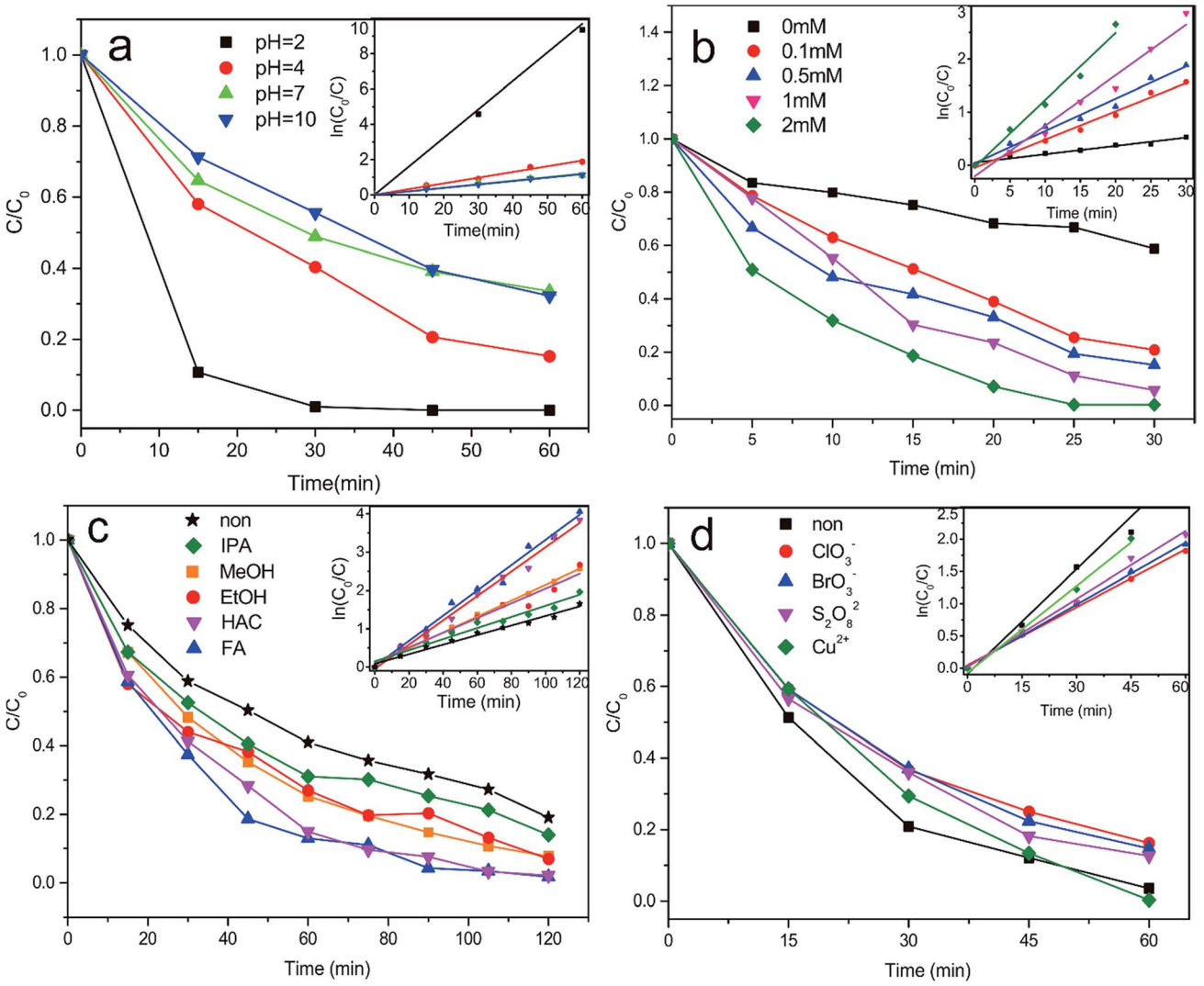

Fig. 5 Effect of various factor on the photocatalytic reduction rate and kinetic of Cr(VI). (a) pH value; (b) the concentration of citric acid; (c) hole scavenger; (d) electron scavenger; experimental conditions: 50 mg L^{-1} initial Cr(VI) concentration, 0.1 g L^{-1} catalyst, pH 2, N_2 purging.

sequence of FA > HAC > EtOH > MeOH > IPA > Non. Moreover, the pseudo-first-order rate constant was further calculated for comparing the promotion of different organic to the reduction rate of Cr(VI).

On the basis of these results, combined with previous reported literature,[48] we suggest that the Cr(VI) reduction rate is affected by organic hole scavenger. In this study, FA was the best candidate due to the fact that FA was a carboxylic acid with larger ionized constant ($pK_a = 3.77$) at pH 3, hence, it was apt to absorb on the positive surface of photocatalyst and would be more susceptible to direct oxidation by the photogenerated holes. Similar explanation can be made on the carboxylic acid of HAC which also had a relative large ionized constant ($pK_a = 4.76$). With respect to MeOH ($pK_a = 15.54$), EtOH ($pK_a = 15.9$) and IPA ($pK_a = 16.5$), the hole scavengers were difficult to ionize and absorb on the photocatalyst surface, resulting in the decrease of Cr(VI) reduction rate.[49–51] Therefore, those organic acid with smaller ionized constant existed in wastewater are beneficial for the Cr(VI) reduction.

3.5.4 Effect of electron scavenger on photocatalytic reduction rate. Compared with the organic acid additives, the inorganic ions which have a reduction potential more positive than the conduction band of photocatalyst can consume the electrons and affect the reduction of Cr(VI) rate. As shown in Fig. 5d, the inhibited effect on reduction rate of Cr(VI) was rather obvious in presence of chlorate, bromate and peroxydisulfate, nevertheless it was not significantly influenced on photocatalytic reduction Cr(VI) in presence of Cu(II). To further demonstrate the extent of inhibiting, the rate constant was calculated. On the basis of previous researches, the decrease of Cr(VI) removal efficiency may be responsible for the competition between electron scavenger and Cr(VI), leading to the decline of the reduction potential and surface adsorption. Similar to the species of Cr(VI), the negative electron scavenger was also inclined to adsorbed onto the surface of catalyst resulting the tentative deactivation of photocatalyst. On the other hand, both the electron scavenger and the species of Cr(VI) could act as the electron acceptor for the photogenerated electrons from the

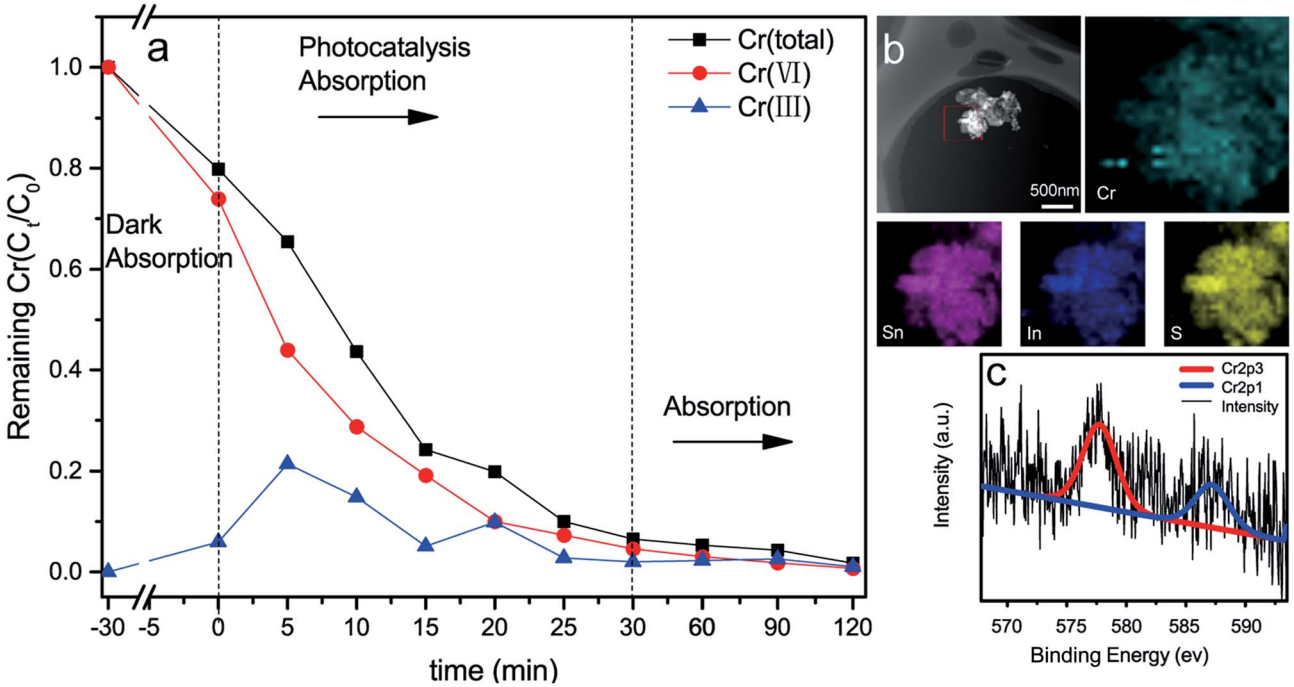

Fig. 6 Synergy of photocatalysis and adsorption of chromium in one-step system. (a) Concentrations of residual Cr(VI) and Cr(III) in solution after photocatalysis and adsorption by rGO/$SnIn_4S_8$; (b) EDS mapping of Cr, Sn, In and S elements on used rGO/$SnIn_4S_8$; (c) high resolution XPS spectrum of Cr 2p; experimental conditions: 5 mg L^{-1} initial Cr(VI) concentration, 0.3 g L^{-1} catalyst, pH 4, N_2 purging, $T = 298$ K.

rGO/$SnIn_4S_8$ nanosheets. According to the experimental result, the order of electron acceptability of the inorganic was as follow: $ClO_3^- < BrO_3^- < S_2O_8^{2-} < Cu^{2+}$.

3.6 Synergy of photocatalysis of Cr(VI) and adsorption of Cr(III)

Previous studies reveal that GO is one of the most effective absorbents for Pb(II), Sb(III) and Cr(III) because of the abundance of O-containing functional groups on the surface of GO nanosheets.[52,53] To investigate the adsorption activity of the rGO/$SnIn_4S_8$, the adsorption of Cr(III) was carried out following by the photocatalysis of Cr(VI). According to the aforementioned XPS results in Fig. 3, the rGO in the rGO/$SnIn_4S_8$ nanosheets still had some hydrophilic groups such as hydroxyl and carboxyl groups despite being hydrothermal reduced. As a result, the rGO could serve as an adsorbent. Experiments on photocatalytic reduction of Cr(VI) was firstly performed. As shown in Fig. 6a, total Cr concentration was decreased with the decreased of Cr(VI) concentration. The removal efficiency of Cr(VI) and total Cr could reach up to a high level of 99.2% and 98.3% within 30 min photocatalysis. It can be calculated that the maximum adsorption capacity of Cr(III) on rGO/$SnIn_4S_8$ surface was about 12.8 mg g^{-1} at pH 4.

After adsorption, the used rGO/$SnIn_4S_8$ nanosheets were separated from the aqueous solution to further subject to EDS and XPS analysis. As illustrated in Fig. 6b, the element of Cr, Sn, In and S was distributed uniformly on the surface of the used nanosheets. Moreover, the chemical state of Cr was investigated by high resolution XPS spectrum and presented in Fig. 6c. Generally, Cr(III) yields two XPS signal with BE peaking at 577.0–578.0 eV and 586.0–588.0 eV, respectively, while the signals of Cr(VI) usually locates between 580.0–580.5 eV and 589.0–590.0 eV.[54] According to the high resolution XPS spectrum of Cr on the surface of rGO/$SnIn_4S_8$ nanosheets, the Cr 2p spectrum exhibited two intense peaks located at 577.7 and 587.1 eV, corresponding to the splitting peak of Cr $2p_{3/2}$ and Cr $2p_{1/2}$, respectively. The spin orbital splitting of Cr $2p_{3/2}$ and Cr $2p_{1/2}$ was 9.4 eV, which was the characteristic peak of Cr(III).

In this system, the Cr(VI) on the surface of rGO/$SnIn_4S_8$ was completely photocatalytic reduction by photogenerated electron, and at the same time the Cr(III) was immediately captured by the rGO owing to the O-containing functional groups on the surface. As a result, chromium in the solution was ultimately transferred to the surface of photocatalyst. That is to say, the synergy of photocatalysis and adsorption played an important role in the complete removal of total chromium.

3.7 Recycling test

It is well known that the photochemically stability is very important for the application of photocatalyst. In this case, the recycling experiment was conducted under similar condition with the initial Cr(VI) concentration of 50 mg L^{-1} at pH 2. Results indicated that the Cr(VI) removal efficiency was up to 95.6% after five cycles, as shown in Fig. S2 (ESI†). Further, XRD analysis and FT-IR spectra before and after 5 times photocatalytic reaction were carried out to investigate the stability of rGo/$SnIn_4S_8$ (see Fig. S3 and S4, ESI†). Careful observation suggested the diffraction peak intensity of XRD pattern and FT-IR spectra of the sample after 5 times tests did not change significantly compared with that of the fresh one, indicating the

high stability of rGO/$SnIn_4S_8$. Consequently, superior photocatalytic reduction efficiency was maintained after repeated use 5 times. Thus, this work might provide a possibility for treating chromium-containing effluent.

4 Conclusions

In summary, 2D rGO/$SnIn_4S_8$ nanosheets were successfully prepared by a simple and economic one-pot surfactant-assisted hydrothermal approach. The as-synthesized nanosheets exhibited excellent photocatalytic ability under visible light, which could reduce Cr(VI) nearly 100% at pH 2 within 30 min in presence of citric acid and retained a relatively high reduction ability, recycle ability and stability after 5 cycles. Moreover, the maximum adsorption capacity of Cr(III) on rGO/$SnIn_4S_8$ surface at pH 4.0 was about 12.8 mg g^{-1}, which provided a promising strategy to ultimately remove chromium from wastewater.

Conflicts of interest

There are no conflicts to declare.

Acknowledgements

The authors gratefully acknowledge the financial support from National Natural Science Foundation of China (grant numbers 21206096 and 21577018) and National Key Research and Development Program of China (2017YFB0308600).

Notes and references

1 M. Owlad, M. K. Aroua, W. A. W. Daud and S. Baroutian, *Water, Air, Soil Pollut.*, 2009, **200**, 59–77.
2 X. Guan, Y. Chen and H. Fan, *ACS Appl. Mater. Interfaces*, 2017, **9**, 15525–15532.
3 J. Yang, K. Yu and C. Liu, *J. Hazard. Mater.*, 2017, **321**, 73–80.
4 V. Suresh, M. Kanthimathi, P. Thanikaivelan, J. R. Rao and B. U. Nair, *J. Cleaner Prod.*, 2001, **9**, 483–491.
5 F. S. Carlos, P. Giovanella, J. Bavaresco, C. D. S. Borges and F. A. D. O. Camargo, *Water, Air, Soil Pollut.*, 2016, **227**, 175–186.
6 D. Mamais, C. Noutsopoulos, I. Kavallari, E. Nyktari, A. Kaldis, E. Panousi, G. Nikitopoulos, K. Antoniou and M. Nasioka, *Chemosphere*, 2016, **152**, 238–244.
7 F. Melak, G. Du Laing, A. Ambelu and E. Alemayehu, *Desalination*, 2016, **377**, 23–27.
8 P. T. Chen, M. Fan, D. Yang, H. He, D. Liu, A. Yuan, J. Zhu and T. Chen, *J. Hazard. Mater.*, 2009, **166**, 821–829.
9 S. Younan, G. Z. Sakita, T. R. Albuquerque, R. Keller and H. Bremer-Neto, *J. Sci. Food Agric.*, 2016, **96**, 3977–3982.
10 P. A. Vinodhini and P. N. Sudha, *Textiles and Clothing Sustainability*, 2017, **2**, 5–20.
11 V. Sureshkumar, S. C. G. Kiruba Daniel, K. Ruckmani and M. Sivakumar, *Appl. Nanosci.*, 2016, **6**, 277–285.
12 C. Liu, N. Fiol, J. Poch and I. Villaescusa, *Journal of Water Process Engineering*, 2016, **11**, 143–151.
13 C. E. Barrera-Díaz, V. Lugo-Lugo and B. Bilyeu, *J. Hazard. Mater.*, 2012, **223–224**, 1–12.
14 N. Wang, L. Zhu, K. Deng, Y. She, Y. Yu and H. Tang, *Appl. Catal., B*, 2010, **95**, 400–407.
15 M. Shirzad-Siboni, M. Farrokhi, R. Darvishi Cheshmeh Soltani, A. Khataee and S. Tajassosi, *Ind. Eng. Chem. Res.*, 2014, **53**, 1079–1087.
16 L. Xu, Y. Wei, W. Guo, Y. Guo and Y. Guo, *Appl. Surf. Sci.*, 2015, **332**, 682–693.
17 S. Jeong, D. Yoo, J. Jang, M. Kim and J. Cheon, *J. Am. Chem. Soc.*, 2012, **134**, 18233–18236.
18 D. Jariwala, V. K. Sangwan, L. J. Lauhon, T. J. Marks and M. C. Hersam, *ACS Nano*, 2014, **8**, 1102–1120.
19 D. Aldakov, A. Lefrançois and P. Reiss, *J. Mater. Chem. C*, 2013, **1**, 3756.
20 F. Deng, X. Lu, L. Zhao, Y. Luo, X. Pei, X. Luo and S. Luo, *J. Mater. Sci.*, 2016, **51**, 6998–7007.
21 W. Liu, J. Cai, Z. Ding and Z. Li, *Appl. Catal., B*, 2015, **174–175**, 421–426.
22 J. Xu, L. Wang and X. Cao, *Chem. Eng. J.*, 2016, 816–825.
23 W. Meng, X. Zhou, Z. Qiu, C. Liu, J. Chen, W. Yue, M. Wang and H. Bi, *Carbon*, 2016, **96**, 532–540.
24 Q. Xiang, J. Yu and M. Jaroniec, *Chem. Soc. Rev.*, 2012, **41**, 782–796.
25 H. R. Thomas, S. P. Day, W. E. Woodruff, C. Vallés, R. J. Young, I. A. Kinloch, G. W. Morley, J. V. Hanna, N. R. Wilson and J. P. Rourke, *Chem. Mater.*, 2013, **25**, 3580–3588.
26 R. K. Upadhyay, N. Soin and S. S. Roy, *RSC Adv.*, 2014, **4**, 3823–3851.
27 D. K. Padhi, T. K. Panigrahi, K. Parida, S. K. Singh and P. M. Mishra, *ACS Sustainable Chem. Eng.*, 2017, **5**, 10551–10562.
28 D. K. Padhi, G. K. Pradhan, K. M. Parida and S. K. Singh, *Chem. Eng. J.*, 2014, **255**, 78–88.
29 D. K. Padhi and K. Parida, *J. Mater. Chem. A*, 2014, **2**, 10300–10312.
30 D. K. Padhi, A. Baral, K. Parida, S. K. Singh and M. K. Ghosh, *J. Phys. Chem. C*, 2017, **121**, 6039–6049.
31 H. Liu, L. Deng, Z. Zhang, J. Guan, Y. Yang and Z. Zhu, *J. Mater. Sci.*, 2015, **50**, 3207–3211.
32 J. H. Kang, T. Kim, J. Choi, J. Park, Y. S. Kim, M. S. Chang, H. Jung, K. T. Park, S. J. Yang and C. R. Park, *Chem. Mater.*, 2016, **28**, 756–764.
33 R. Vinoth, P. Karthik, C. Muthamizhchelvan, B. Neppolian and M. Ashokkumar, *Phys. Chem. Chem. Phys.*, 2016, **18**, 5179–5191.
34 J. Cai, W. Liu and Z. Li, *Appl. Surf. Sci.*, 2015, **358**, 146–151.
35 S. Yang, L. Li, Z. Pei, C. Li, J. Lv, J. Xie, B. Wen and S. Zhang, *Colloids Surf., A*, 2014, **457**, 100–106.
36 D. S. Kim and S. Kwak, *Appl. Catal., A*, 2007, **323**, 110–118.
37 M. Thommes, K. Kaneko, A. V. Neimark, J. P. Olivier, F. Rodriguez-Reinoso, J. Rouquerol and K. S. W. Sing, *Pure Appl. Chem.*, 2015, **87**, 1051–1069.
38 J. Tauc, R. Grigorovict and A. Vancu, *Phys. Status Solidi*, 1966, **15**, 627–637.

39 L. Wang, X. Li, W. Teng, Q. Zhao, Y. Shi, R. Yue and Y. Chen, *J. Hazard. Mater.*, 2013, **244–245**, 681–688.
40 M. Radecka, M. Rekas, A. Trenczek-Zajac and K. Zakrzewska, *J. Power Sources*, 2008, **181**, 46–55.
41 L. G. Arriaga and A. M. Fernández, *Int. J. Hydrogen Energy*, 2002, **27**, 27–31.
42 K. Kabra, R. Chaudhary and R. L. Sawhney, *J. Hazard. Mater.*, 2007, **149**, 680–685.
43 S. Luo, Y. Xiao, L. Yang, C. Liu, F. Su, Y. Li, Q. Cai and G. Zeng, *Sep. Purif. Technol.*, 2011, **79**, 85–91.
44 K. M. Parida and N. Sahu, *J. Mol. Catal. A: Chem.*, 2008, **287**, 151–158.
45 J. Yoon, E. Shim, S. Bae and H. Joo, *J. Hazard. Mater.*, 2009, **161**, 1069–1074.
46 L. Yang, Y. Xiao, S. Liu, Y. Li, Q. Cai, S. Luo and G. Zeng, *Appl. Catal., B*, 2010, **94**, 142–149.
47 P. Zhou, J. Yu and M. Jaroniec, *Adv. Mater.*, 2014, **26**, 4920–4935.
48 R. Marks, T. Yang, P. Westerhoff and K. Doudrick, *Water Res.*, 2016, **104**, 11–19.
49 R. Lucchetti, A. Siciliano, L. Clarizia, D. Russo, I. Di Somma, F. Di Natale, M. Guida, R. Andreozzi and R. Marotta, *Environ. Sci. Pollut. Res.*, 2017, **24**, 5898–5907.
50 K. Doudrick, T. Yang, K. Hristovski and P. Westerhoff, *Appl. Catal., B*, 2013, **136–137**, 40–47.
51 T. Tan, D. Beydoun and R. Amal, *J. Photochem. Photobiol., A*, 2003, **159**, 273–280.
52 Q. Chang, S. Song, Y. Wang, J. Li and J. Ma, *Anal. Methods*, 2012, **4**, 1110.
53 Y. Leng, W. Guo, S. Su, C. Yi and L. Xing, *Chem. Eng. J.*, 2012, **211–212**, 406–411.
54 X. Guan, J. Chang, Z. Xu, Y. Chen and H. Fan, *RSC Adv.*, 2016, **6**, 29054–29063.